ADVANCED FUNCTIONAL MATERIALS
www.afm-journal.de

Check for updates

Pinning of the Fermi Level in $CuFeO_2$ by Polaron Formation Limiting the Photovoltage for Photochemical Water Splitting

Yannick Hermans, Andreas Klein, Hori Pada Sarker, Mohammad N. Huda, Henrik Junge, Thierry Toupance, and Wolfram Jaegermann**

$CuFeO_2$ is recognized as a potential photocathode for photo(electro)-chemical water splitting. However, photocurrents with $CuFeO_2$-based systems are rather low so far. In order to optimize charge carrier separation and water reduction kinetics, defined $CuFeO_2$/Pt, $CuFeO_2$/Ag, and $CuFeO_2/NiO_x(OH)_y$ heterostructures are made in this work through a photodeposition procedure based on a 2H $CuFeO_2$ hexagonal nanoplatelet shaped powder. However, water splitting performance tests in a closed batch photoreactor show that these heterostructured powders exhibit limited water reduction efficiencies. To test whether Fermi level pinning intrinsically limits the water reduction capacity of $CuFeO_2$, the Fermi level tunability in $CuFeO_2$ is evaluated by creating $CuFeO_2$/ITO and $CuFeO_2/H_2O$ interfaces and analyzing the electronic and chemical properties of the interfaces through photoelectron spectroscopy. The results indicate that Fermi level pinning at the Fe^{3+}/Fe^{2+} electron polaron formation level may intrinsically prohibit $CuFeO_2$ from acquiring enough photovoltage to reach the water reduction potential. This result is complemented with density functional theory calculations as well.

1. Introduction

Photo(electro)chemical (PEC) water splitting is a promising method to produce hydrogen in a sustainable, cost-effective, and environmentally friendly way. To perform water splitting with a PEC device, a photovoltage of at least 1.7 V (1.23 V standard water splitting potential + overvoltages) has to be generated by one or more photoabsorbers immersed in an aqueous electrolyte. With regards to cost and practical feasibility a dual bed particle suspension PEC reactor, wherein one type of photoabsorber particle should initiate the water oxidation reaction H_2O/O_2 and another should perform the water reduction reaction H^+/H_2, was regarded as the PEC reactor with the highest potential to be economically competitive to conventional fossil fuel-based hydrogen production methods.[1] However, for such type of photochemical water splitting reactors, lab scale solar-to-hydrogen (STH) conversion efficiencies of only 1% have been measured so far.[2,3]

One way to increase the STH conversion efficiency is to improve the efficiency of the water reduction reaction, in which $CuFeO_2$ could play a promising role. $CuFeO_2$ is an intrinsic p-type semiconductor with a delafossite crystal structure, made up by a stacking of alternating $[Cu^+]$ and $[FeO^{2-}]$ layers perpendicular to the *c*-axis. Two polytypes, 3R with rhombohedral symmetry and 2H with hexagonal symmetry, have been associated with the $CuFeO_2$ delafossite crystal structure. Because 2H $CuFeO_2$ cannot be easily synthesized, only 3R $CuFeO_2$ has been studied extensively so far. The suitability of 3R $CuFeO_2$ for water reduction stems from its appropriate

Dr. Y. Hermans, Prof. W. Jaegermann
Surface Science
TU Darmstadt
Otto-Berndt-Str. 3, 64287 Darmstadt, Germany
E-mail: yhermans@surface.tu-darmstadt.de;
jaegermann@surface.tu-darmstadt.de

The ORCID identification number(s) for the author(s) of this article can be found under https://doi.org/10.1002/adfm.201910432.

© 2020 The Authors. Published by WILEY-VCH Verlag GmbH & Co. KGaA, Weinheim. This is an open access article under the terms of the Creative Commons Attribution-NonCommercial-NoDerivs License, which permits use and distribution in any medium, provided the original work is properly cited, the use is non-commercial and no modifications or adaptations are made.

DOI: 10.1002/adfm.201910432

Dr. Y. Hermans, Prof. T. Toupance
Molecular Chemistry and Materials
Univ. Bordeaux, ISM, UMR 5255 CNRS
351 Cours de la Libération F-33405, Talence Cedex, France
Prof. A. Klein
Electronic Structure of Materials
TU Darmstadt
Otto-Berndt-Str. 3, 64287 Darmstadt, Germany
H. P. Sarker, Prof. M. N. Huda
Department of Physics
University of Texas at Arlington
Arlington, TX 76019, USA
Dr. H. Junge
Leibniz-Institut für Katalyse e.V.
Universität Rostock
Albert-Einstein-Str. 29a, 18059 Rostock, Germany

properties such as its reduced bandgap of 1.5 eV,[4,5] its suitable conduction band minimum, which allows for water reduction,[4–7] its good carrier mobility of about 0.2 $cm^2 V^{-1} s^{-1}$,[5] and because it is composed of earth-abundant elements.

Despite these good properties which should allow theoretically for photocurrents up to 15 mA cm^{-2},[5] poor to mediocre hydrogen evolution efficiencies have been measured so far for 3R $CuFeO_2$. The only fairly reasonable photocurrent was found by Jang et al. at 2.4 mA cm^{-2} at 0.4 V versus RHE for a 3R $CuFeO_2$ photocathode, which was modified through hybrid microwave annealing and contained a NiFe-layered double hydroxide/reduced graphene oxide electrocatalyst.[8] Also Prévot et al. demonstrated photocurrents of up to 2.4 mA cm^{-2} for a host–guest $CuAlO_2/CuFeO_2$ system, however using oxygen as an electron scavenger, so that water splitting could not be assumed any more.[9] To the best of our knowledge, no higher photocurrents or hydrogen evolution efficiencies have been reported up to now. It is also worth underlying that the efficiencies mentioned above have all been determined under an applied bias, meaning that unbiased hydrogen evolution with 3R $CuFeO_2$ has seemingly not been achieved yet. Several reasons have been suggested to explain why $CuFeO_2$ has only shown low hydrogen evolution efficiencies so far, which include photocorrosion,[4] poor catalytic activity,[8] Fermi level (E_F) pinning at bandgap states in the bulk,[10] and Fermi level pinning at surface states.[5] Upward Fermi level pinning has also recently been found for other iron containing oxides such as hematite (α-Fe_2O_3) and $BiFeO_3$, and has been linked to the transition of Fe^{3+} to Fe^{2+}.[11,12]

If poor catalytic activity would be limiting the PEC water splitting efficiency of $CuFeO_2$, an appropriate solution would be the creation of a heterostructure, by attaching a water reduction cocatalyst onto $CuFeO_2$.[13] Besides enhanced kinetics,[14] a heterostructure may also improve charge carrier separation[15,16] and surface passivation.[17] For water reduction, platinum has been recognized as an efficient cocatalyst.[14,18,19] To further enhance the advantages of heterostructures a facet-selective photodeposition process may be used to create an anisotropic heterostructured powder. Li et al. have shown that anisotropic $SrTiO_3$ and $BiVO_4$ heterostructured powders could be synthesized through a photodeposition process using anisotropic $SrTiO_3$ and $BiVO_4$ powders with two different kinds of exposed facets.[20–22] Moreover, these anisotropic heterostructures exhibited improved water splitting efficiencies with respect to heterostructures with randomly deposited cocatalysts, because of a suggested synergistic charge carrier separation–cocatalyst effect.

In this work we tested whether the creation of anisotropic heterostructures could boost the water reduction properties of $CuFeO_2$. Since, the rhombohedral 3R polytype does not allow for the creation of anisotropic particles we opted to synthesize anisotropic hexagonal 2H $CuFeO_2$ nanoplatelets according to a recently published procedure.[23] Next, we tested whether Pt, Ag, and $NiO_x(OH)_y$ could be selectively deposited onto specific facets of the 2H $CuFeO_2$ nanoplatelets and analyzed whether the resulting heterostructures improve the $CuFeO_2$ water reduction efficiency. However, no substantial improvements in water reduction could be achieved. Therefore, we additionally tested whether Fermi level pinning could be the reason for the weak photocatalytic properties of $CuFeO_2$ by performing so-called interface experiments, in which the electronic and chemical properties of a developing interface are studied using photoelectron spectroscopy.[24] In particular, we studied by how much we could increase the Fermi level by contacting 2H $CuFeO_2$ pellets with a low work function material, $Sn:In_2O_3$ (ITO), as this should lead to downward band bending. Additionally, the influence of water on the surface electronic properties of 2H $CuFeO_2$ was investigated. Only limited downward band bendings for both $CuFeO_2$/ITO and $CuFeO_2$/H_2O interfaces, as well as the reduction of Fe^{3+} to Fe^{2+} were observed. These results potentially indicate a bulk Fermi level pinning phenomenon at the Fe^{3+}/Fe^{2+} charge transition level.

2. Results and Discussion

2.1. Synthesis and Characterization of Anisotropic Heterostructured 2H $CuFeO_2$ Nanoplatelets

2H $CuFeO_2$ hexagonal nanoplatelets were prepared by scaling-up and optimizing a recently published synthetic procedure.[23] Secondary electron microscopy (SEM) images depicted in **Figure 1**a,b show that the synthesized $CuFeO_2$ powders exhibit the hexagonal nanoplatelet morphology. The large hexagonal top faces of the particles correspond to the {0001} crystalline facets, while the exact facets corresponding to the side faces of the nanoplatelets are less clear due to the sides being seemingly rounded. Most likely, the sides of the particles consist of the prismatic {1-101} facets, while {01-10} facets might be present as well. The X-ray powder diffractograms show that the $CuFeO_2$ powder mainly consists of 2H $CuFeO_2$ as well as a small amount of rhombohedral 3R $CuFeO_2$ (Figure S1, Supporting Information). In the remainder of the paper the synthesized $CuFeO_2$ powder is referred to as 2H $CuFeO_2$.

Ag, Pt, and $NiO_x(OH)_y$ were deposited onto the 2H $CuFeO_2$ nanoplatelets through a photodeposition process and characterized by field emission secondary electron microscopy (FESEM) (Figure 1c–f). The secondary electron image and back scatter electron image displayed in Figure 1c,d, respectively, demonstrate that the photodeposition of Pt led to a selective deposition of Pt on the {0001} facets, creating an anisotropic heterostructured $CuFeO_2$/Pt powder. The photodeposition of Ag on 2H $CuFeO_2$ also seems to have led to the selective deposition of Ag on the {0001} 2H $CuFeO_2$ facets (Figure 1e). The size of the silver deposit is rather large, which indicates that growth dominates over nucleation. As a result, the 2H $CuFeO_2$ particles only contain up to a few silver particles per facet. By contrast, the $NiO_x(OH)_y$ photodeposition does not seem to exhibit any particular regioselectivity, because a deposit can be observed over the entirety of the 2H $CuFeO_2$ particles as indicated by FESEM images (Figure 1f). The anisotropic photodeposition of Pt and Ag onto anisotropic particles has been observed before for $SrTiO_3$ and $BiVO_4$.[20,21] The anisotropic photodeposition might be caused by dissimilar band bending across the different exposed facets, as measurements on single crystals suggest.[25,26] However, highly anisotropic electrical conductivities perpendicular and parallel to the *c*-axis, as observed for 3R $CuFeO_2$ single crystals,[27] might also be the reason for the observed anisotropic photodeposition.

Auger electron spectroscopy (AES) was then performed to determine the chemical nature of the deposits seen in the FESEM images. The AES measurements were performed on

© 2020 The Authors. Published by WILEY-VCH Verlag GmbH & Co. KGaA, Weinheim

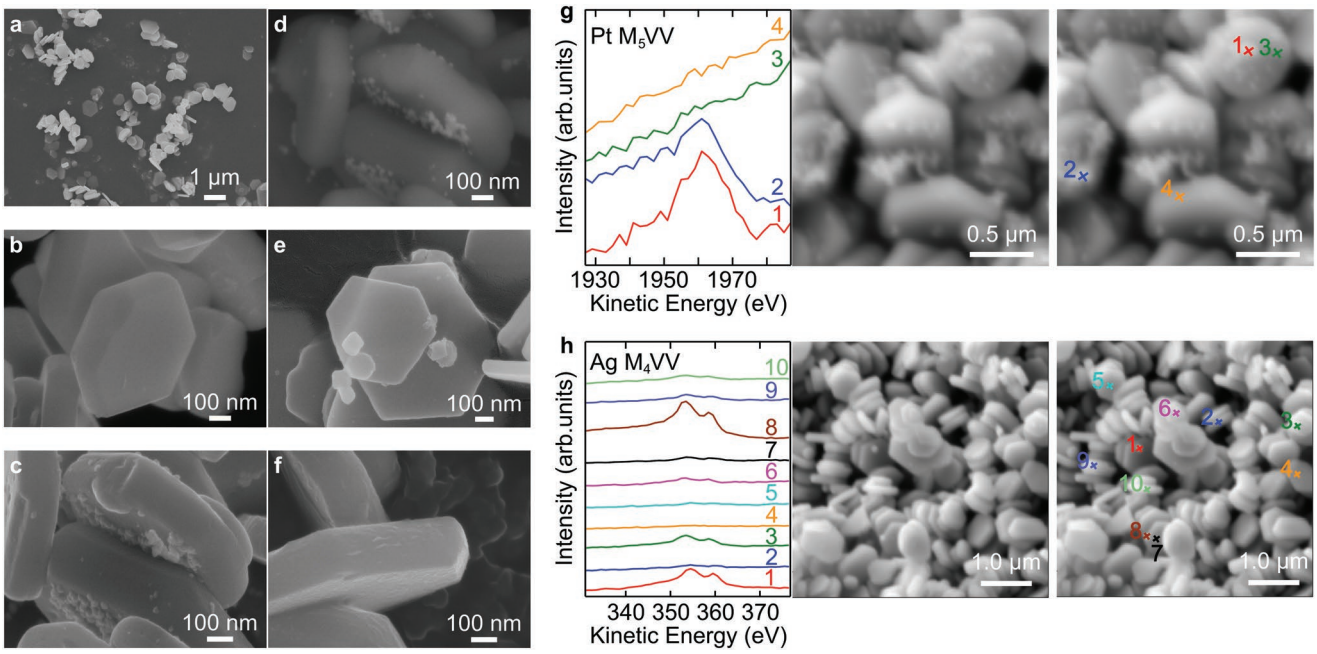

Figure 1. a,b) Secondary electron microscopy (SEM) images of 2H $CuFeO_2$, c) $CuFeO_2$/Pt, e) $CuFeO_2$/Ag, f) $CuFeO_2/NiO_x(OH)_y$. d) Back-scattered electron (BSE) image of $CuFeO_2$/Pt. g) Pt N_7VV Auger electron spectroscopy (AES) point measurements on $CuFeO_2$/Pt. h) Ag M_4VV AES point measurements on $CuFeO_2$/Pt. The crosses in the SEM images taken with the AES setup indicate the AES measurement points. The Pt and Ag content is 10 wt% and the Ni content is 1 wt%.

specific points on the heterostructured particles which were selected according to newly recorded secondary electron images with the AES setup. The Pt M_5VV Auger electron spectra in Figure 1g confirm that the deposit seen in the FESEM images of the $CuFeO_2$/Pt sample corresponds to platinum, because a clear Pt M_5VV Auger signal can be seen for measurements on points with a visible deposit. Similarly, Auger electron spectra for the $CuFeO_2$/Ag sample recorded on deposits visible in the secondary electron images resulted in clear Ag M_4VV emissions (Figure 1h). AES could not be used to identify Ni in the $CuFeO_2/NiO_x(OH)_y$ powders, because of the low loading of nickel and the overlap of the Ni Auger emission lines with the Auger emission lines of iron and copper.

The chemical state of the deposits was further investigated by X-ray photoelectron spectroscopy (XPS) (**Figure 2**). In the Pt 4f spectrum of the $CuFeO_2$/Pt sample two intense signals at 71.0 and 74.4 eV can be seen which are characteristic for the binding energies of Pt $4f_{7/2}$ and Pt $4f_{5/2}$, respectively, of metallic platinum.[28] Additionally, a shoulder can be seen at a binding energy of 77.4 eV, which is indicative of Pt $4f_{5/2}$ of platinum oxide.[28] Platinum oxide can be formed when the $[PtCl_6]^{2-}$ platinum precursor hydrolyses or only partially reduces during the photodeposition process.[29–31] The Ag 3d of $CuFeO_2$/Ag consists of two signals at 368.2 and 374.3 eV, which belong to the characteristic binding energies of Ag $3d_{5/2}$ and Ag $3d_{3/2}$, respectively, of metallic silver,[28] thus proving that the silver photodeposition involves the reduction of Ag^+ to Ag(0). Based on the Ni 2p line shape of $CuFeO_2/NiO_x(OH)_y$, a pure NiO species can be excluded as nickel deposit, since that would have given rise to a noticeable peak splitting of the main Ni $2p_{3/2}$ line at a binding energy around 856.5 eV,[32] which is not seen in our Ni 2p spectra. Instead, the Ni 2p line shape resembles more that of a mixed nickel oxyhydroxide.[32,33] Furthermore, in the O 1s core level X-ray photoelectron (XP) spectrum of the $CuFeO_2/NiO_x(OH)_y$ sample (Figure S2, Supporting Information), a strong signal at a binding energy of 532.1 eV can be seen. This signal corresponds to hydroxides and is typical for samples prepared under ambient conditions, as these conditions promote the adsorption of carbohydrates and water onto the exposed samples. However, the signal here is considerably stronger than usual and

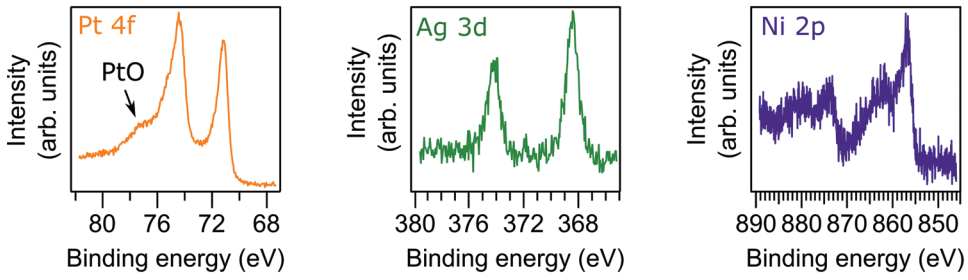

Figure 2. Pt 4f, Ag 3d, and Ni 2p core level XP spectra of $CuFeO_2$/Pt (10 wt%), $CuFeO_2$/Ag (10 wt%), and $CuFeO_2/NiO_x(OH)_y$ (±10 wt%), respectively.

© 2020 The Authors. Published by WILEY-VCH Verlag GmbH & Co. KGaA, Weinheim

approximately as strong as the O^{2-} signal at a binding energy of 530.3 eV, thus indicating the presence of another hydroxide species such as nickel hydroxides.[28,33] Therefore, the deposited nickel species is denoted as $NiO_x(OH)_y$ in the following.

Next, the sacrificial water splitting efficiency of the 2H $CuFeO_2$ heterostructured powders was tested. However, none of the heterostructured 2H $CuFeO_2$ powders demonstrated any significant gas evolution, despite the presence of suitable contact materials. Even platinum, which is considered to be the state of the art hydrogen evolution catalyst,[14] did not allow for any measureable gas evolution. Anyhow, the gas composition in the reactor after the sacrificial water splitting experiments was probed by gas chromatography. Here, hydrogen was detected for the $CuFeO_2$/Pt heterostructured powders, but the signal corresponded to a hydrogen evolution rate of <500 nmol h^{-1} (Figure S3, Supporting Information). For $CuFeO_2$/Ag and $CuFeO_2$/$NiO_x(OH)_y$ no hydrogen could be detected.

2.2. Interface Experiments to Determine Fermi Level Pinning in 2H $CuFeO_2$

The inability of any of the heterostructured 2H $CuFeO_2$ powders to produce high amounts of hydrogen through sacrificial water splitting is a remarkable phenomenon. Recently, Prévot et al. showed through a set of photoelectrochemical measurements with varied redox systems that 3R $CuFeO_2$ thin films suffer from Fermi level pinning at a defect level positioned at about 0.7 eV versus normal hydrogen electrode (NHE).[5] According to the authors the Fermi level pinning was due to surface states caused by a metal hydroxide surface layer. To test whether Fermi level pinning was the main cause of the limited sacrificial water reduction efficiencies of our 2H $CuFeO_2$ nanoplatelet powders, we performed so-called interface experiments following the Kraut method.[24] In such an interface experiment a thin film is sputtered in a stepwise fashion onto a substrate, performing photoelectron spectroscopy measurements in between each deposition step. By making the interface with a low work function material, Sn:In_2O_3 (ITO), upward band bending should be obtained, which can be derived from the binding energy shifts of core and valence band spectra.

Interface experiments are mostly performed with thin film substrates to avoid sample charging during XPS measurements, which may happen for weakly conductive semiconductors. However, since 3R $CuFeO_2$ reportedly has a relatively good conductivity,[5] we assumed that pellets made from our bare 2H $CuFeO_2$ powders, could be used as substrates. In Figure S4 of the Supporting Information the X-ray diffractogram of 2H $CuFeO_2$ powder and pellet are compared. It does not seem that new phases have been formed. However the {0001} orientation increased, most likely because uniaxial pressing aligned the nanoplatelets along the exposed {0001} facets. To prepare the $CuFeO_2$ pellets for the interface experiments the surface was cleaned with distilled water, followed by a heating step in O_2 to remove the extrinsic contamination layer. Indeed, in Figure S5 of the Supporting Information the survey XP spectrum of the 2H $CuFeO_2$ pellet before and after heating in O_2 atmosphere shows that carbon is effectively removed. After the heating step a sodium signal appears, which we attributed to the surface accumulation of sodium present in the pellets due to the powder being synthesized in 40 equivalents of NaOH. However, the small amount of residual sodium is unlikely to influence the interface experiment.

This surface cleaned 2H $CuFeO_2$ substrate was then used in an interface experiment with ITO (**Figure 3**). During the interface experiment, the developing $CuFeO_2$/ITO interface can be clearly followed through the photoelectron spectroscopy measurements, as the intensity of the Cu 2p, Fe 2p, and Cu LMM spectra (Figure 3a) decrease and the In $3d_{5/2}$ intensity increases with increasing ITO sputtering time. Meanwhile, the O 1s intensity remains constant. Since the Cu 2p, Cu LMM, Fe 2p, and valence band spectra shift simultaneously toward higher binding energies with increasing ITO coverage, the shift is rather due to a change in electronic properties and not due to a change in the chemical structure. As the Fermi level to valence band maximum distance (E_F–E_{VBM}) of bare 2H $CuFeO_2$ is quite low, the ITO valence band spectrum does not overlap with that of 2H $CuFeO_2$, so that the shift in the 2H $CuFeO_2$ valence band maximum (VBM) can be used to quantify the electronic shift. Quantifying the shift by following the shift in the Cu LMM and Fe $2p_{3/2}$ is more complicated, because of the asymmetric line shape in both spectra and, additionally, the large number of satellites and overlap of In $3p_{1/2}$ and Sn $3p_{3/2}$ lines in the Fe $2p_{3/2}$ spectra. The Cu $2p_{3/2}$ binding energy shift can be followed with ease due to its relatively strong intensity and well-defined line shape. The Cu $2p_{3/2}$ and E_F–E_{VBM} binding energy shifts with respect to ITO deposition time are shown in Figure S6 of the Supporting Information. For the VBM and Cu $2p_{3/2}$ spectra an upward binding energy shift of 0.32 and 0.37 eV, respectively, is obtained. A second interface experiment showed very similar shifts of 0.37 and 0.44 eV for VBM and Cu $2p_{3/2}$, respectively.

Difference spectra of Cu $2p_{3/2}$, Cu LMM, and Fe $2p_{3/2}$ were made (Figure 3b) to verify whether the ITO interface experiment led to any chemical changes in $CuFeO_2$. In the Cu $2p_{3/2}$ core level spectrum a broadening of the main Cu $2p_{3/2}$ line can be seen. The broadening of the principal Cu $2p_{3/2}$ line, seen here, most likely does not correspond to an oxidation of Cu^+ to Cu^{2+}, because then an increase in intensity in the satellite region between 940 and 945 eV, characteristic for Cu^{2+}, should be seen as well.[34] Furthermore, the Cu LMM Auger spectrum after 4 s of ITO deposition does not show any sign of Cu^{2+} either, as then a signal should appear at a 0.9 eV lower binding energy with respect to the main Cu^+ Cu LMM line.[35] In addition, a change from Cu^+ to Cu^{2+} is not consistent with the observed increase in Cu LMM binding energy. The increase in binding energies could lead to the reduction of Cu^+ to Cu(0), which would, however, lead to reduction of the Cu $2p_{3/2}$ line width as well as the appearance of a signal in the Cu LMM spectrum.[36] Hence, the broadening of the main Cu $2p_{3/2}$ line is not likely due to a change in the copper oxidation state. Another possible reason for the increased broadening of the main Cu $2p_{3/2}$ line is inhomogeneous ITO coverage due to the large substrate surface roughness, which is plausible for a powder pressed pellet. In this case, the Cu $2p_{3/2}$ line at 4 s ITO coverage would then be a composite signal consisting of Cu $2p_{3/2}$ signals with different binding energy shifts, originating from positions with differing ITO thickness. However, the Cu LMM and Fe $2p_{3/2}$ spectrum apparently do not suffer from line broadening, which would be expected if surface roughness was the cause of Cu

© 2020 The Authors. Published by WILEY-VCH Verlag GmbH & Co. KGaA, Weinheim

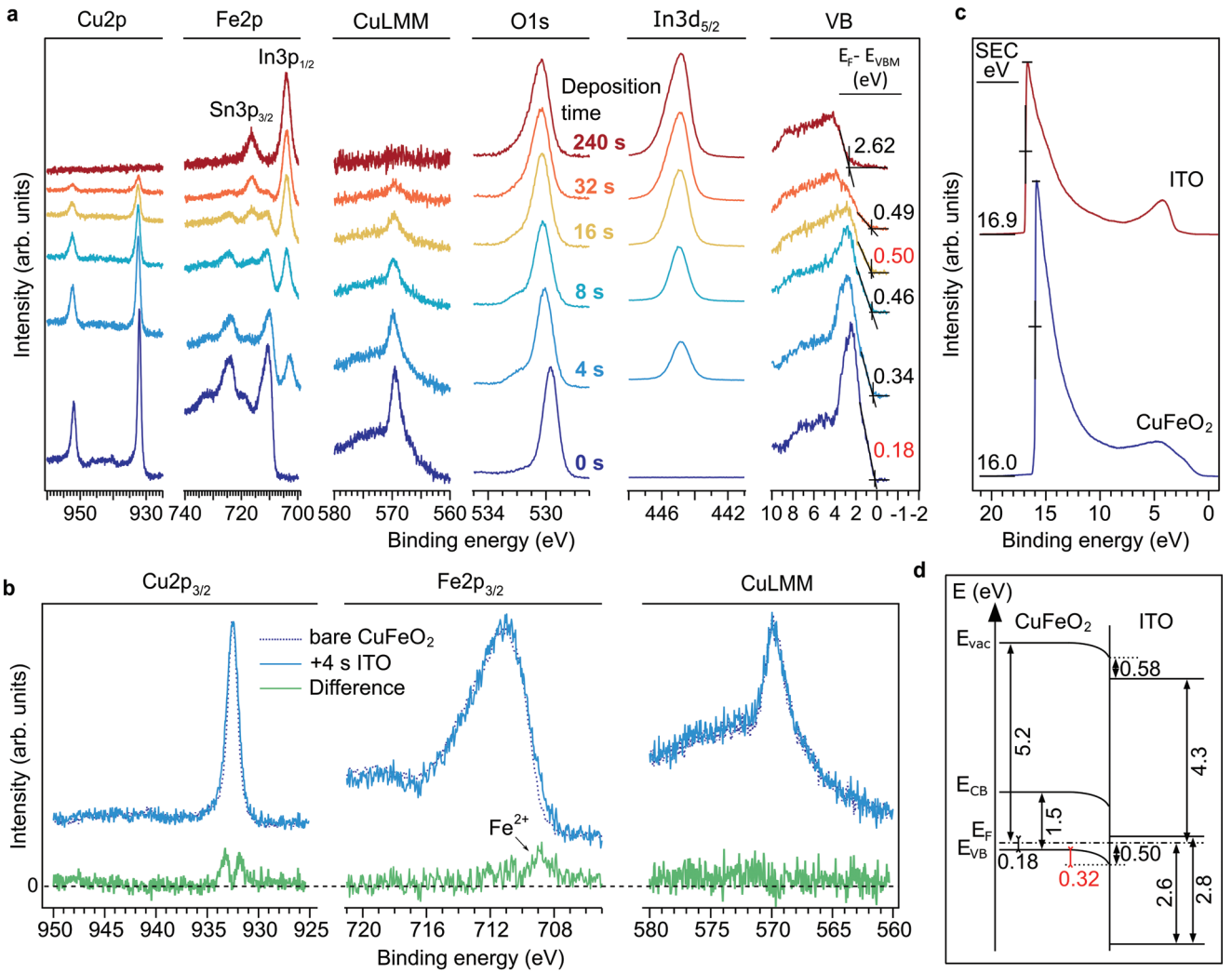

Figure 3. a) Cu 2p, Fe 2p, Cu LMM, O 1s, In $3d_{5/2}$ core level, and valence band (VB) XP spectra, and Cu LMM Auger spectra for the $CuFeO_2$/ITO interface experiment. The ITO deposition times are denoted in the graph. b) Difference spectra of Cu $2p_{3/2}$, Cu LMM, and Fe $2p_{3/2}$ between bare $CuFeO_2$ and $CuFeO_2$/ITO (4 s). Shirley background subtraction was done for Cu 2p and Tougaard background subtraction for Fe 2p. The spectra were normalized and the spectra measured after 4 s of ITO deposition are shifted in binding energy so that they match the binding energy of the spectra of bare $CuFeO_2$. c) UP spectra of the $CuFeO_2$ substrate (blue) and the ITO film (yellow) after a deposition time of 240 s, including the secondary electron cut-offs (SEC). d) Energy band diagram of $CuFeO_2$/ITO with all energy values denoted in eV and the bandgap of ITO taken from literature.[40]

$2p_{3/2}$ line broadening. Therefore, the exact cause of the Cu $2p_{3/2}$ line broadening could not be unambiguously determined.

More importantly, an extra signal at lower binding energy, around 709 eV, appears in the Fe $2p_{3/2}$ difference spectra after 4 s of ITO deposition (Figure 3b). Since this binding energy position is characteristic for Fe^{2+},[37] Fe^{3+} is likely partly reduced to Fe^{2+}, in response to the ITO coverage. Moreover, in our group the appearance of Fe^{2+} in the Fe $2p_{3/2}$ spectrum has been observed before for hematite,[11] while increasing the Fermi level position through ITO deposition.

From the secondary electron cut-offs of the measured ultraviolet photoelectron (UP) spectra (Figure 3c), work functions of 5.2 and 4.3 eV were determined for the 2H $CuFeO_2$ pellet and the ITO film, respectively. The ITO work function, here, corresponds to earlier published ITO work functions.[38,39] When combining the 5.2 eV $CuFeO_2$ work function with the value of 0.2 eV for E_F–E_{VBM}, an ionization potential of 5.4 eV is retrieved for the 2H $CuFeO_2$ pellet. Indeed, Omeiri et al. determined through Mott–Schottky flat band measurements that the ionization potential of the (001) surface of a 3R $CuFeO_2$ single crystal amounts to 5.4 eV.[6] Due to the Mott–Schottky measurements being performed at the point of zero charge, the similarity of the $CuFeO_2$ surfaces and the similarity of the ionization potentials, the presence of a strong surface dipole at the 2H $CuFeO_2$ pellet surface is regarded as being unlikely.

The results of the $CuFeO_2$/ITO interface experiment are summarized in a band diagram in Figure 3d, with the band gap of ITO taken from literature.[40] The band diagram shows that there is a staggered type II band alignment between ITO and $CuFeO_2$, where, upon light absorption, electrons would flow toward ITO due to the downward band bending. A vacuum level offset of 0.58 eV can be seen, which can be caused by a surface dipole

© 2020 The Authors. Published by WILEY-VCH Verlag GmbH & Co. KGaA, Weinheim

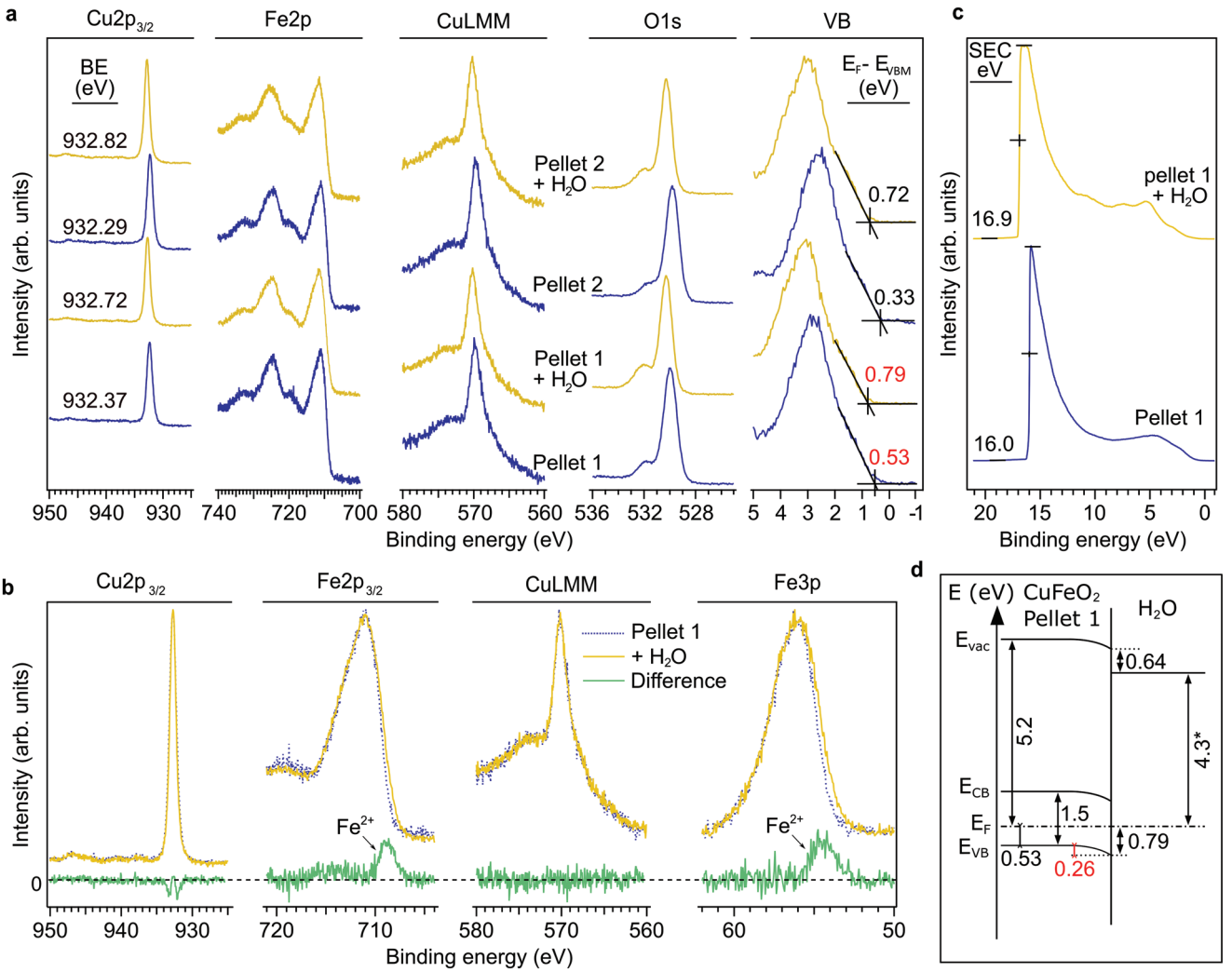

Figure 4. a) Cu $2p_{3/2}$, Fe 2p, O 1s core level, and valence band XP spectra and Cu LMM Auger spectrum of two thermally cleaned (200 °C, O_2, 5 h) 2H $CuFeO_2$ pellets before (blue) and after (yellow) water exposure. b) Difference spectra (green) of Cu $2p_{3/2}$, Fe $2p_{3/2}$, Cu LMM, and Fe 3p between 2H $CuFeO_2$ pellet 1 before (blue) and after (yellow) water exposure. Shirley background subtraction was performed for Cu 2p and Fe 3p, and Tougaard background subtraction for Fe 2p. The spectra were normalized and the spectra measured after water exposure are shifted in binding energy so that they match the binding energy of the spectra of bare $CuFeO_2$. c) UP spectra of 2H $CuFeO_2$ pellet 1 before (blue) and after (yellow) water exposure, including the secondary electron cut-offs (SEC). d) Energy band diagram of $CuFeO_2/H_2O$ with all energy values denoted in eV. * work function of $CuFeO_2$ after water adsorption, not of water itself.

or by Fermi level pinning. The possibility of a surface dipole at the 2H $CuFeO_2$ surface can be cautiously neglected, because (as discussed above) the 2H $CuFeO_2$ pellet ionization potential corresponds well to that of a (001) exposed 3R $CuFeO_2$ single crystal determined at the point of zero charge under flat band conditions.[6] Contrarily, the 4.3 eV ITO work function is quite low, considering the value of 2.6 eV for E_F–E_{VBM} (Figure 3a). However, this work function agrees well with other values of ITO films deposited at room temperature.[38,41] Another possible reason for the observed vacuum level offset could be Fermi level pinning.

To validate the potential Fermi level pinning effect observed in the $CuFeO_2$/ITO interface experiment, another kind of interface experiment was performed by exposing a cleaned 2H $CuFeO_2$ substrate surface (Figure S7, Supporting Information) to water, also denoted as water exposure experiment. The interface with water was expected to increase the E_F–E_{VBM} of $CuFeO_2$ further, because of the low work functions that can be obtained after water exposure.[26,42] The effect of water exposure on the Cu $2p_{3/2}$, Fe 2p, O 1s, and valence band XP and Cu LMM Auger spectra of $CuFeO_2$ is shown in **Figure 4**a. All spectra shift toward higher binding energies upon water exposure, as would be expected from an interface experiment with a low work function material. Moreover, water exposure led to a higher binding energy shift compared to ITO, as the E_F–E_{VBM} shifted toward 0.7–0.8 eV. Admittedly, the Fermi level of pellet 1 before water exposure was already positioned at a quite high position, likely caused by a different amount of doping or inhomogeneous surface charging. In the O 1s spectra an additional feature at a binding energy of 532 eV can be seen, which is characteristic for carbonyl bonds and hydroxides.[28] After water exposure this signal at 532 eV increases, indicating that additional hydroxides were formed during water exposure.[43] The

© 2020 The Authors. Published by WILEY-VCH Verlag GmbH & Co. KGaA, Weinheim

appearance of an hydroxylated surface upon water exposure has been observed before for other Fe oxide surfaces, such as Fe_3O_4(001),[44] α-Fe_2O_3(0001),[45–47] and α-Fe_2O_3(1-102).[48] The relative intensity ratios of the core level spectra depicted in Table S1 of the Supporting Information show that changes in the oxygen, iron, and copper content are negligible.

Difference spectra of Cu $2p_{3/2}$, Fe $2p_{3/2}$, Cu LMM, and Fe 3p (Figure 4b) were generated to verify whether the exposure of 2H $CuFeO_2$ to water led to any chemical changes. In the difference trace of the main Cu $2p_{3/2}$ signal an apparent line narrowing can be seen. As a possible effect, Cu^{2+}, which may be present in small amounts, reduces to Cu^{+}, which is, however, unlikely as no changes are noticed in the Cu $2p_{3/2}$ satellite region.[34] Another possibility is the reduction of Cu^{+} to Cu(0), which is also unlikely since then an extra signal at lower binding energy in the Cu LMM spectra should appear.[34] Hence, just as for the line broadening observed after ITO deposition no clear explanation can be deduced for the main Cu $2p_{3/2}$ line width change. Both Fe $2p_{3/2}$ and Fe 3p core level spectra exhibit an extra signal at lower binding energy after water exposure, which indicates the presence of Fe^{2+}.[37,49] The Fe^{2+} signal is also somewhat more intense than what was seen for the $CuFeO_2$/ITO interface.

Figure 4c displays the UP spectra of 2H $CuFeO_2$ pellet 1 before and after water exposure. First of all, the upward binding energy shift induced by the water exposure can also be noticed in the VB region of the UP spectra. Second, the work function of the $CuFeO_2$ pellets before water exposure, 5.2 eV, corresponds to what was found earlier and after water exposure a work function shift toward 4.3–4.4 eV can be noticed. This work function shift could be related to the adsorption of water onto the porous $CuFeO_2$ pellet. The adsorption of water is seemingly confirmed by the valence band region in the UP spectra. After water exposure, features at 5.3, 7.4, and 11.2 eV can be seen, which are characteristic to the $1b_1$, $3a_1$, and $1b_2$ orbitals, respectively, of molecular water, only shifted by about 2 eV.[50] The shift could be due to the water being physisorbed to the 2H $CuFeO_2$ substrate, as a 1 eV shift with respect to molecular water was seen earlier for physisorbed water on NiO.[43]

In Figure 4d the resulting band diagram of 2H $CuFeO_2$ pellet 1 is shown. As can be seen, the E_F–E_{VBM} increases up to 0.8 eV after the water exposure. Therefore, the 0.5 eV E_F–E_{VBM} observed for the $CuFeO_2$/ITO interface experiment does not seem to be a fixed limit. The 4.3 eV work function indicated in the figure correspond to that of the $CuFeO_2$ pellet after the water exposure and not to water itself.

Both the $CuFeO_2$/ITO interface experiment and the $CuFeO_2$/H_2O water exposure experiment led to an electron injection process into $CuFeO_2$, which led to an increase of the Fermi level up to a certain point and a reduction of Fe^{3+} to Fe^{2+}. To investigate the origin of the reduction of iron theoretical density functional theory calculations were made in which an extra electron was added to $CuFeO_2$.

2.3. Electron Polaron Calculation in 2H $CuFeO_2$

In transition metal oxides, the conduction band minimum consists of empty d-bands. Electrons can get localized to form electron polarons by filling up these empty d^n states.[51] In $CuFeO_2$,

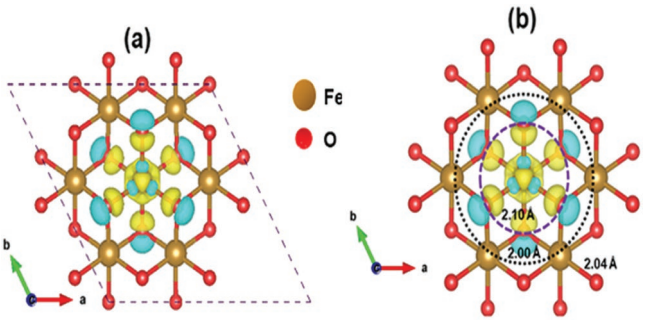

Figure 5. a) Charge density difference plot of a localized electron polaron in an Fe site. The charge difference is taken between the cell containing an extra electron and the cell without this extra electron. The charge density difference plot is drawn using an isosurface value of 0.025 $eÅ^{-3}$. Blue regions indicate decreased charge density, while yellow regions indicate increased charge density. b) Geometry of local lattice distortion due to electron polaron formation. The Fe—O bond length elongation and shortening around the Fe^{2+} site is indicated by the purple and black circles, respectively. The equilibrium Fe—O bond length is 2.04 Å.

there are unoccupied Fe 3d orbitals around the conduction band minimum (CBM).[52] Thus, when an extra electron is supplied to the $CuFeO_2$ matrix (either by photoexcitation or by injection from the surroundings), the excess electron may get trapped on an Fe lattice site by filling up the unoccupied Fe 3d orbitals, resulting in an electron polaron and the reduction of the formerly Fe^{3+} lattice site to Fe^{2+}. We used two theoretical methods, called footprints in the following, to characterize polaron formation within the 2H $CuFeO_2$ matrix. The footprints are i) localized electron density and ii) local lattice distortion. i) **Figure 5**a shows the charge density difference plot of a 2H $CuFeO_2$ cell containing an extra electron and the cell without this extra electron. The extra electron is situated in the Fe lattice site as indicated by the yellow isosurface. Most of the electron wave function is in the Fe site but a small portion is also present in the nearby O sites. ii) Additionally, the extra electron is associated with a local lattice distortion around the reduced Fe^{2+} site in the first shell as indicated by the purple colored circle in Figure 5b. Fe^{2+}—O bonds are more elongated (by about 0.06 Å) than the equilibrium Fe^{3+}—O bonds. The Fe^{2+}—O bond elongation is attributed to the Coulomb repulsion due to the extra electron on the Fe site. On the other hand, for the 1st nearest neighbor Fe atoms around the reduced Fe^{2+} site, the Fe^{3+}—O bond length shortens (by about 0.04 Å) compared to the equilibrium Fe—O bond length in the 2nd shell as indicated by the black colored circle. The other Fe—O and Cu—O bond lengths (outside the 2nd shell) remain unchanged. These results are most likely transferable to 3R $CuFeO_2$ since bond lengths between nearest neighbors are largely maintained between 3R and 2H Cu-delafossites.[53,54]

2.4. Fermi Level Tunability in $CuFeO_2$

The results of the $CuFeO_2$/ITO interface experiment and the $CuFeO_2$ water exposure experiment are summarized in **Figure 6**. Figure 6a shows the range of Fermi level positions that were obtained after calcining the 2H $CuFeO_2$ pellets and after establishing the interfaces of 2H $CuFeO_2$ with water and ITO. According to literature, the VBM of 3R $CuFeO_2$ is situated

© 2020 The Authors. Published by WILEY-VCH Verlag GmbH & Co. KGaA, Weinheim

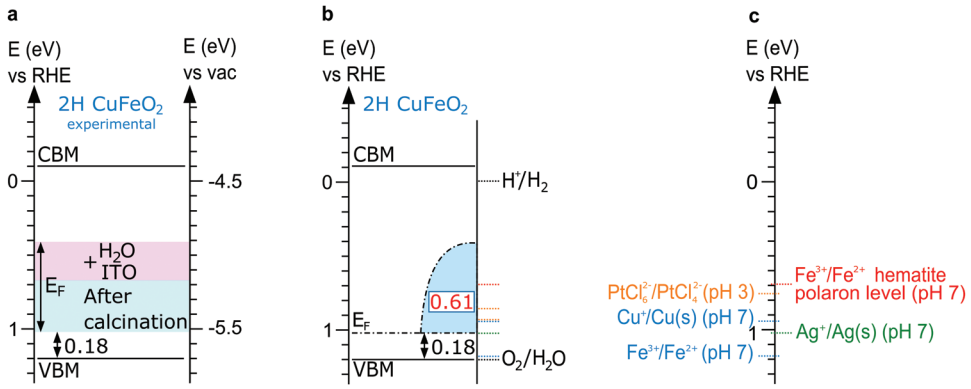

Figure 6. a) Diagram showing the experimental Fermi level ranges after calcinations and after interface formation. b) Diagram showing the Fermi level tunability in 2H $CuFeO_2$ based on the $CuFeO_2$/ITO interface experiment and the $CuFeO_2$ water exposure experiment. c) A series of reduction potentials calculated at particular pH values on the RHE scale. Bandgap taken from literature.[23] 3R $CuFeO_2$ VBM position also taken from literature.[5,7]

between 1.0 –1.4 eV versus RHE and the CBM should be within –0.1 to –0.5 eV versus RHE.[4–7] For 2H $CuFeO_2$ a similar valence band position can be assumed due to the similarity of the VBM of Cu-delafossites in general[55] as well of that of different polytypes.[56,57] However, a small difference in the bandgap may exist between 2H $CuFeO_2$ and 3R $CuFeO_2$, which are reported to be about 1.33[23] and 1.45 eV.[10,52] The apparent Fermi level tunability range amounts to 0.61 eV, as determined from the $CuFeO_2$/ITO interface experiment and the $CuFeO_2$ water exposure experiments. According to these experiments, the E_F of 2H $CuFeO_2$ could be increased up to 0.8 eV above the VBM and the Fe 2p XP core level spectra indicated the reduction of Fe^{3+} to Fe^{2+} upon contact with ITO and H_2O. Moreover, the theoretical calculations described above indicated as well that excess electrons occupy Fe lattice sites in $CuFeO_2$.

The experimental Fermi level tunability range (Figure 6b) can be compared to a series of standard reduction potentials (Figure 6c). The Fe^{3+}/Fe^{2+} (pH 7) aqueous reduction potential at about 1.18 eV versus RHE, cannot explain the induced Fe^{3+} reduction at the $CuFeO_2$/ITO contact, as this reduction potential would mean that the iron would already be in the Fe^{2+} state for bare $CuFeO_2$ because of its Fermi level position at about 1.02 eV versus RHE. However, the Fe^{3+} coordination in solution and in the 2H $CuFeO_2$ crystal lattice differs from one another, meaning that the actual Fe^{3+}/Fe^{2+} charge transition level in 2H $CuFeO_2$ probably does not correspond to the Fe^{3+}/Fe^{2+} aqueous reduction potential. Lohaus et al. found that electron polaron formation limits the Fermi level tunability within hematite (Fe_2O_3).[11] Experimentally, the authors demonstrated that the Fe^{3+}/Fe^{2+} charge transition level for hematite, which has a similar octahedral iron coordination as 2H $CuFeO_2$, lies at about 0.3 eV versus NHE, which on the RHE scale will be 0.7 eV versus RHE (pH 7). This position would fit to our experiments due to the appearance of Fe^{2+} in the Fe 2p spectra for Fermi level positions below 0.7 eV versus RHE. Additionally, the polaron formation at Fe sites in hematite is also what we derived from our theoretical calculations. Recently, the Fe^{3+}/Fe^{2+} charge transition level at about 0.7 eV versus RHE (pH 7) was also found for $BiFeO_3$ by Bein et al.[12] Furthermore, Prévot et al. observed as well Fermi level pinning in 3R $CuFeO_2$ at about 0.7 eV versus RHE (pH 7), which the authors assumed to be caused by surface states.[5] Possibly, the Fermi level pinning phenomenon that the authors observed, was not due to surface states but due to the formation and occupation of the bulk Fe^{3+}/Fe^{2+} polaron level. Proof for this assumption are the similarities in the observed Fermi level pinning positions in our and Prévot's experiments, the similar octahedral Fe coordination in both polytypes and the limited differences in the 3R and 2H electronic structure of other Cu delafossites.[57] The pinning at the Fe^{3+}/Fe^{2+} charge transition level, thus, seems to be a general phenomenon for Fe oxides. The 0.8 eV E_F–E_{VBM} energy distance that we could obtain in our experiments corresponds to an $E_{F,max}$ position of about 0.4 eV versus RHE, which is still far from reaching the water reduction potential at 0 eV versus RHE. As such, the bulk Fe^{3+}/Fe^{2+} polaron level may be the reason for the low sacrificial water splitting efficiency of the heterostructured 2H $CuFeO_2$ powders, because pinning at the Fe^{3+}/Fe^{2+} polaron level may inhibit the generation of enough photovoltage to drive the water reduction reaction. Additionally, the pinning at the Fe^{3+}/Fe^{2+} polaron level would be a problem for which no solution may be engineered because it would be intrinsic to $CuFeO_2$.

Because the $PtCl_6^{2-}/PtCl_4^{2-}$ (0.75 eV vs RHE) and $Ag^+/Ag(0)$ (1.02 eV versus RHE) reduction potentials lie well within the range in which the Fermi level can be tuned, $PtCl_6^{2-}$ and Ag^+ are allowed to be reduced by $CuFeO_2$, upon light absorption, as observed in our photodeposition experiments. Also the oxygen reduction reaction, which is often used to assess the reducing capacity of $CuFeO_2$ samples,[9,58] is allowed, because its standard reduction potential at 1.23 eV versus RHE lies well below the $E_{F,max}$ at about 0.4 eV versus RHE.

3. Conclusion

In conclusion, we have shown that Ag and Pt could be selectively deposited onto the {0001} facets of a hexagonal nanoplatelet shaped 2H $CuFeO_2$ powder through photodeposition. The photodeposition of $NiO_x(OH)_y$ did not show any selectivity for a particular facet. Unfortunately, none of the heterostructured 2H $CuFeO_2$ powders could produce any significant amount of hydrogen through sacrificial water reduction, which is an indication of an intrinsic limitation of $CuFeO_2$. This was further investigated through interface experiments. Specifically,

© 2020 The Authors. Published by WILEY-VCH Verlag GmbH & Co. KGaA, Weinheim

the $CuFeO_2$/ITO and $CuFeO_2/H_2O$ interface was studied. For both $CuFeO_2$/ITO and $CuFeO_2/H_2O$ the E_F–E_{VBM} could be increased up to 0.5 and 0.8 eV, respectively. Additionally, the presence of Fe^{2+} was detected for both interface experiments, being more present for the $CuFeO_2/H_2O$ interface. Therefore, an increasing Fermi level position could lead to a higher occupation of the Fe^{3+}/Fe^{2+} electron polaron level, which may limit the amount of photovoltage that can be reached with $CuFeO_2$. Indeed, the maximum 0.8 eV E_F–E_{VBM} that we could achieve correspond to a Fermi level position of 0.4 eV versus RHE which is still far from the water reduction potential of 0 eV versus RHE. Because the earlier determined Fermi level tunability of hematite (Fe_2O_3) was also evidently limited by the Fe^{3+}/Fe^{2+} charge transition level at 0.7 eV versus RHE (pH 7), one may ask whether the incorporation of iron in compounds intended for unbiased water reduction should be avoided.

Supporting Information

Supporting Information is available from the Wiley Online Library or from the author.

Acknowledgements

This work was carried out in the framework of EJD-FunMat (European Joint Doctorate for Multifunctional Materials) and has received funding from the European Union's Horizon 2020 research and innovation program under the Marie Sklodowska-Curie Grant Agreement No. 641640. M.N.H. was supported by the National Science Foundation (Award No. DMR-1609811). H.P.S. and M.N.H. thank the Texas Advanced Computing Center (Austin, TX) for their computational needs.

Conflict of Interest

The authors declare no conflict of interest.

Keywords

$CuFeO_2$, Fermi level pinning, photocatalysis, photoelectron spectroscopy, water splitting

Received: December 16, 2019
Published online: January 20, 2020

[1] B. A. Pinaud, J. D. Benck, L. C. Seitz, A. J. Forman, Z. Chen, T. G. Deutsch, B. D. James, K. N. Baum, G. N. Baum, S. Ardo, H. Wang, E. Miller, T. F. Jaramillo, *Energy Environ. Sci.* **2013**, *6*, 1983.
[2] Q. Wang, T. Hisatomi, Q. Jia, H. Tokudome, M. Zhong, C. Wang, Z. Pan, T. Takata, M. Nakabayashi, N. Shibata, Y. Li, I. D. Sharp, A. Kudo, T. Yamada, K. Domen, *Nat. Mater.* **2016**, *15*, 611.
[3] Q. Wang, T. Hisatomi, Y. Suzuki, Z. Pan, J. Seo, M. Katayama, T. Minegishi, H. Nishiyama, T. Takata, K. Seki, A. Kudo, T. Yamada, K. Domen, *J. Am. Chem. Soc.* **2017**, *139*, 1675.
[4] C. G. Read, Y. Park, K.-S. Choi, *J. Phys. Chem. Lett.* **2012**, *3*, 1872.
[5] M. S. Prévot, X. A. Jeanbourquin, W. S. Bourée, F. Abdi, D. Friedrich, R. van de Krol, N. Guijarro, F. Le Formal, K. Sivula, *Chem. Mater.* **2017**, *29*, 4952.
[6] S. Omeiri, B. Bellal, A. Bouguelia, Y. Bessekhouad, M. Trari, *J. Solid State Electrochem.* **2009**, *13*, 1395.
[7] K. Sivula, R. van de Krol, *Nat. Rev. Mater.* **2016**, *1*, 15010.
[8] Y. J. Jang, Y. Bin Park, H. E. Kim, Y. H. Choi, S. H. Choi, J. S. Lee, *Chem. Mater.* **2016**, *28*, 6054.
[9] M. S. Prévot, Y. Li, N. Guijarro, K. Sivula, *J. Mater. Chem. A* **2016**, *4*, 3018.
[10] M. S. Prévot, N. Guijarro, K. Sivula, *ChemSusChem* **2015**, *8*, 1359.
[11] C. Lohaus, A. Klein, W. Jaegermann, *Nat. Commun.* **2018**, *9*, 4309.
[12] N. S. Bein, P. Machado, M. Coll, F. Chen, M. Makarovic, T. Rojac, A. Klein, *J. Phys. Chem. Lett.* **2019**, *10*, 7071.
[13] A. Kudo, Y. Miseki, *Chem. Soc. Rev.* **2009**, *38*, 253.
[14] C. C. L. McCrory, S. Jung, I. M. Ferrer, S. M. Chatman, J. C. Peters, T. F. Jaramillo, *J. Am. Chem. Soc.* **2015**, *137*, 4347.
[15] M. Barroso, A. J. Cowan, S. R. Pendlebury, M. Grätzel, D. R. Klug, J. R. Durrant, *J. Am. Chem. Soc.* **2011**, *133*, 14868.
[16] Y. Hermans, S. Murcia-López, A. Klein, R. van de Krol, T. Andreu, J. R. Morante, T. Toupance, W. Jaegermann, *Phys. Chem. Chem. Phys.* **2019**, *21*, 5086.
[17] C. Zachäus, F. F. Abdi, L. M. Peter, R. van de Krol, *Chem. Sci.* **2017**, *8*, 3712.
[18] F. E. Osterloh, *Chem. Mater.* **2008**, *20*, 35.
[19] N. P. Dasgupta, C. Liu, S. Andrews, F. B. Prinz, P. Yang, *J. Am. Chem. Soc.* **2013**, *135*, 12932.
[20] R. Li, F. Zhang, D. Wang, J. Yang, M. Li, J. Zhu, X. Zhou, H. Han, C. Li, *Nat. Commun.* **2013**, *4*, 1432.
[21] L. Mu, Y. Zhao, A. Li, S. Wang, Z. Wang, J. Yang, Y. Wang, T. Liu, R. Chen, J. Zhu, F. Fan, R. Li, C. Li, *Energy Environ. Sci.* **2016**, *9*, 2463.
[22] R. Li, H. Han, F. Zhang, D. Wang, C. Li, *Energy Environ. Sci.* **2014**, *7*, 1369.
[23] Y. Jin, G. Chumanov, *RSC Adv.* **2016**, *6*, 26392.
[24] J. R. Waldrop, E. A. Kraut, S. P. Kowalczyk, R. W. Grant, *Surf. Sci.* **1983**, *132*, 513.
[25] J. Zhu, F. Fan, R. Chen, H. An, Z. Feng, C. Li, *Angew. Chem., Int. Ed.* **2015**, *54*, 9111.
[26] S. Kashiwaya, J. Morasch, V. Streibel, T. Toupance, W. Jaegermann, A. Klein, *Surfaces* **2018**, *1*, 73.
[27] R. D. Shannon, D. B. Rogers, C. T. Prewitt, J. L. Gillson, *Inorg. Chem.* **1971**, *10*, 723.
[28] J. F. Moulder, W. F. Stickle, P. E. Sobol, K. D. Bomben, *Handbook of X-Ray Photoelectron Spectroscopy: A Reference Book of Standard Spectra for Identification and Interpretation of XPS Data*, Physical Electronics, Eden Prairie, MN **1992**.
[29] C. Xi, Z. Chen, Q. Li, Z. Jin, *J. Photochem. Photobiol., A* **1995**, *87*, 249.
[30] K. Wenderich, G. Mul, *Chem. Rev.* **2016**, *116*, 14587.
[31] D. C. Harris, *Quantitative Chemical Analysis*, W. H. Freeman, New York **2015**.
[32] A. P. Grosvenor, M. C. Biesinger, R. S. C. Smart, N. S. McIntyre, *Surf. Sci.* **2006**, *600*, 1771.
[33] N. Weidler, J. Schuch, F. Knaus, P. Stenner, S. Hoch, A. Maljusch, R. Schäfer, B. Kaiser, W. Jaegermann, *J. Phys. Chem. C* **2017**, *121*, 6455.
[34] M. C. Biesinger, L. W. M. Lau, A. R. Gerson, R. S. C. Smart, *Appl. Surf. Sci.* **2010**, *257*, 887.
[35] S. Poulston, P. M. Parlett, P. Stone, M. Bowker, *Surf. Interface Anal.* **1996**, *24*, 811.
[36] M. C. Biesinger, *Surf. Interface Anal.* **2017**, *49*, 1325.
[37] M. C. Biesinger, B. P. Payne, A. P. Grosvenor, L. W. M. Lau, A. R. Gerson, R. S. C. Smart, *Appl. Surf. Sci.* **2011**, *257*, 2717.
[38] Y. Hermans, A. Klein, K. Ellmer, R. van de Krol, T. Toupance, W. Jaegermann, *J. Phys. Chem. C* **2018**, *122*, 20861.
[39] Y. Gassenbauer, A. Klein, *J. Phys. Chem. B* **2006**, *110*, 4793.

© 2020 The Authors. Published by WILEY-VCH Verlag GmbH & Co. KGaA, Weinheim

[40] A. Walsh, J. L. F. Da Silva, S. H. Wei, C. Körber, A. Klein, L. F. J. Piper, A. Demasi, K. E. Smith, G. Panaccione, P. Torelli, D. J. Payne, A. Bourlange, R. G. Egdell, *Phys. Rev. Lett.* **2008**, *100*, 167402.
[41] A. Klein, C. Körber, A. Wachau, F. Säuberlich, Y. Gassenbauer, S. P. Harvey, D. E. Proffit, T. O. Mason, *Materials* **2010**, *3*, 4892.
[42] Y. Joseph, C. Kuhrs, W. Ranke, M. Ritter, W. Weiss, *Chem. Phys. Lett.* **1999**, *314*, 195.
[43] M. Fingerle, S. Tengeler, W. Calvet, T. Mayer, W. Jaegermann, *J. Electrochem. Soc.* **2018**, *165*, H3148.
[44] T. Kendelewicz, S. Kaya, J. T. Newberg, H. Bluhm, N. Mulakaluri, W. Moritz, M. Scheffler, A. Nilsson, R. Pentcheva, G. E. Brown, *J. Phys. Chem. C* **2013**, *117*, 2719.
[45] R. L. Kurtz, V. E. Henrich, *Phys. Rev. B* **1987**, *36*, 3413.
[46] L. Schöttner, R. Ovcharenko, A. Nefedov, E. Voloshina, Y. Wang, J. Sauer, C. Wöll, *J. Phys. Chem. C* **2019**, *123*, 8324.
[47] S. Yamamoto, T. Kendelewicz, J. T. Newberg, G. Ketteler, D. E. Starr, E. R. Mysak, K. J. Andersson, H. Ogasawara, H. Bluhm, M. Salmeron, G. E. Brown, A. Nilsson, *J. Phys. Chem. C* **2010**, *114*, 2256.
[48] M. A. Henderson, *Surf. Sci. Rep.* **2002**, *46*, 1.
[49] A. P. Grosvenor, B. A. Kobe, M. C. Biesinger, N. S. McIntyre, *Surf. Interface Anal.* **2004**, *36*, 1564.
[50] P. A. Thiel, T. E. Madey, *Surf. Sci. Rep.* **1987**, *7*, 211.
[51] A. J. E. Rettie, W. D. Chemelewski, D. Emin, C. B. Mullins, *J. Phys. Chem. Lett.* **2016**, *7*, 471.
[52] C.-M. Jiang, S. E. Reyes-Lillo, Y. Liang, Y.-S. Liu, G. Liu, F. M. Toma, D. Prendergast, I. D. Sharp, J. K. Cooper, *Chem. Mater.* **2019**, *31*, 2524.
[53] J. Li, A. F. Yokochi, A. W. Sleight, *Solid State Sci.* **2004**, *6*, 831.
[54] A. Buljan, P. Alemany, E. Ruiz, *J. Phys. Chem. B* **1999**, *103*, 8060.
[55] K. Rajeshwar, M. K. Hossain, R. T. Macaluso, C. Janáky, A. Varga, P. J. Kulesza, *J. Electrochem. Soc.* **2018**, *165*, H3192.
[56] V. V. Afanas'ev, M. Bassler, G. Pensl, M. J. Schulz, E. Stein von Kamienski, *J. Appl. Phys.* **1996**, *79*, 3108.
[57] M. N. Huda, Y. Yan, A. Walsh, S.-H. Wei, M. M. Al-Jassim, *Phys. Rev. B* **2009**, *80*, 035205.
[58] S.-Y. Zhao, B. Zhang, H. Su, J.-J. Zhang, X.-H. Li, K.-X. Wang, J.-S. Chen, X. Wei, P. Feng, *J. Mater. Chem. A* **2018**, *6*, 4331.

© 2020 The Authors. Published by WILEY-VCH Verlag GmbH & Co. KGaA, Weinheim